Matter and Radiation at Extremes | RESEARCH ARTICLE | scitation.org/journal/mre

Characterization of the stability and dynamics of a laser-produced plasma expanding across a strong magnetic field

Cite as: Matter Radiat. Extremes 7, 026903 (2022); doi: 10.1063/5.0058306
Submitted: 28 May 2021 • Accepted: 16 February 2022 •
Published Online: 11 March 2022

Weipeng Yao,[1,2,a] Julien Capitaine,[2] Benjamin Khiar,[3] Tommaso Vinci,[1] Konstantin Burdonov,[1,2,4] Jérôme Béard,[5] Julien Fuchs,[1] and Andrea Ciardi[2]

AFFILIATIONS

[1]LULI–CNRS, CEA, Sorbonne Université, Ecole Polytechnique, Institut Polytechnique de Paris, F-91128 Palaiseau cedex, France
[2]Sorbonne Université, Observatoire de Paris, Université PSL, CNRS, LERMA, F-75005 Paris, France
[3]Office National d'Etudes et de Recherches Aérospatiales (ONERA), F-91123 Palaiseau, France
[4]IAP, Russian Academy of Sciences, 603950 Nizhny Novgorod, Russia
[5]LNCMI, UPR 3228, CNRS-UGA-UPS-INSA, F-31400 Toulouse, France

Note: This paper is part of the Special Issue on Magnetized Plasmas in HEDP.
[a]**Author to whom correspondence should be addressed:** yao.weipeng@polytechnique.edu

ABSTRACT

Magnetized laser-produced plasmas are central to many studies in laboratory astrophysics, in inertial confinement fusion, and in industrial applications. Here, we present the results of large-scale three-dimensional magnetohydrodynamic simulations of the dynamics of a laser-produced plasma expanding into a transverse magnetic field with a strength of tens of teslas. The simulations show the plasma being confined by the strong magnetic field into a slender slab structured by the magnetized Rayleigh–Taylor instability that develops at the plasma–vacuum interface. We find that when the initial velocity of the plume is perturbed, the slab can develop kink-like motions that disrupt its propagation.

I. INTRODUCTION

Plasma flows across magnetic fields occur throughout the Universe.[1] The stability and dynamics of such plasma flows are of paramount importance in understanding the deceleration, trapping, and heating of plasmas in magnetic fields.

Thanks to the development of high-power lasers coupled to high-strength magnetic field devices,[2,3] we are now able to investigate the interaction between plasmas and strong magnetic fields in the laboratory in a controllable and well-diagnosed environment.[4–10] In addition, in the context of inertial confinement fusion (ICF), there is increasing need for a detailed understanding of plasma dynamics in the presence of strong magnetic fields,[11–13] such as for cross-magnetic-field transport processes.[14]

As well as the strength of the applied magnetic field, its relative direction (with respect to the plasma flow) plays an important role in the stability and dynamics of these plasmas. For example, in an axisymmetric scenario (when the two directions are aligned with each other), the plasma expansion is collimated into a stable jet.[15–17] However, in the case of a magnetic field transverse to the plasma flow, both stable[18] and unstable[19] flows have been reported in the literature, and there is not yet a clear understanding or detailed characterization of this issue. In the following, we briefly review previous studies of the interaction between laser-produced plasmas and transverse magnetic fields before detailing our present contribution.

Over the past few decades, much effort has been devoted to investigating the overall dynamics of the expansion of a laser-produced plasma across a magnetic field. We should note that as our understanding of the underlying physics has progressed over time, this has been accompanied by progress in experimental capabilities, namely, the available laser energy and magnetic field strength. To the best of our knowledge, the earliest laboratory investigations on this subject can be traced back to the early 1970s,[20,21] when the laser energies that could be achieved were up to 2.4 J and the magnetic field strength was ≲6 T. In these experiments, both plasma confinement and flow across the magnetic field were observed. The

flow was explained, from a kinetic point of view, as $\mathbf{E} \times \mathbf{B}$ drift, in which the electric field $\mathbf{E}$ was the result of charge separation at the front of the expanding plasma. Notably, no instabilities were observed.

When the available laser energy increased to about 7 J, some "wings" were revealed at the leading edge of the plasma, and a number of "ripples" inside the plasma were observed,[22] which drew attention to the issue of instabilities. At higher laser energies, ~30 J, flute-mode instabilities (i.e., modes with wave vector perpendicular to the external magnetic field) were observed and carefully analyzed.[23–25] In addition, bifurcation or splitting of the flute tips was observed during the nonlinear phase of the instability. It was also reported that the characteristic wavelength of the flute-like structure was approximately independent of the magnetic field strength.[19] These instabilities have been attributed to lower hybrid drift instability (LHDI),[26,27] because of the large ion Larmor radius (>2 cm) and the relatively low collisionality associated with the low plasma densities produced ($<10^{14}$ cm^{-3}). Furthermore, as the laser energy increased, besides the LHDI, other modes of plasma instability were proposed, namely, electron–ion hybrid instability,[28] unmagnetized Rayleigh–Taylor instability,[29,30] and large-Larmor-radius instability.[31]

Note that in the above pioneering works, the magnetic fields were no more than tens of teslas for laser energies of tens of joules. In fact, if the laser energy is increased further but the magnetic field strength is not, the plasma will no longer be confined within the characteristic spatial and temporal scales of the experiment.[15] Thus, laser energies of a few tens of joules and magnetic field strengths up to few tens of teslas are the parameter ranges we focus on here. In addition, owing to the limited availability of diagnostics in these early works, the plasma density, ionization state, temperature, and local magnetic field strength could not be assessed precisely. Since these are necessary to accurately characterize both the laser-produced plasma and the magnetic field environment, it was hard to pinpoint the precise mechanism (kinetic or fluid) and thereby understand the plasma propagation across the magnetic field and its dynamics. A large increase in the magnetic field strength was realized by using pulsed power generators to achieve up to 17 T, but no instabilities were observed in these experiments, at least in the plane perpendicular to the magnetic field, where the observations were made.[32]

Recently, a detailed picture of the interaction between a laser-produced plasma flow and a strong transverse magnetic field was presented.[33] The plasma plume was observed to be confined into a slender, rapidly elongating slab, and was structured by the magnetized Rayleigh–Taylor instability (MRTI).

In spite of these efforts, a comprehensive study of the 3D dynamics of the plasma over long time and spatial scales is still lacking. Here, we provide the first such characterization using a large-scale 3D resistive-MHD simulation with the GORGON code.[34,35]

The remainder of the paper is organized as follows. In Sec. II, we present our numerical model and simulation setup. Then, in Sec. III, we detail the overall evolution of the plasma plume and characterize the key parameters in detail. In Sec. III A, we investigate how slab formation can be affected when stronger magnetic fields are applied. In Secs. III B and III C, we analyze the possible reasons for the disruptions of the plasma slab propagation (provided a strong enough magnetic field is applied) with two different simulation cases: asymmetric and Bessel-like laser energy deposition patterns. Finally, we give our conclusions in Sec. IV.

II. NUMERICAL SETUP

We simulate the typical laser conditions of experiments performed on the ELFIE laser.[4,13,16,33] A schematic of the simulation setup is shown in Fig. 1. The solid Teflon (C_2F_4) target (in gray) is irradiated with a laser pulse (in red) with 17 J energy, 0.5 ns pulse duration at full-width half-maximum (FWHM), and 1.057 μm laser wavelength. The focal spot is Gaussian with a FWHM diameter of 750 μm, and the on-target intensity is about 7.7×10^{12} W/cm^2. The angle of the laser incidence on the Teflon target in the experiments is 10°.[36] The magnetic field (in blue) is uniformly applied along the x direction, with $B_x = 30$ T, and we will focus on the evolution of the plasma plume (in orange).

The simulation box is defined by a uniform Cartesian grid of dimensions $8 \times 8 \times 30$ mm^3, the number of cells is $400 \times 400 \times 1500 = 2.4 \times 10^8$, the spatial resolution is $dx = dy = dz = 20$ μm, and the simulation duration is 50 ns. Both the box size (along the z direction) and the simulation duration are increased compared with those in our previous paper[33] in order to investigate late-time slab propagation. We here consider "outflow" boundary conditions. GORGON solves the resistive MHD equations, uses a vector potential formalism, and retains the displacement current in vacuum. This allows the code to model a computational vacuum whose cutoff density is set to 10^{-4} kg/m^3.

The interaction between the laser and the solid target is simulated using the DUED code,[37] which solves the single-fluid three-temperature equations in two-dimensional axisymmetric cylindrical geometry in Lagrangian form. The code uses the material properties of a two-temperature equation of state (EOS) model incorporating solid state effects, and a multigroup flux-limited radiation transport module with tabulated opacities. The laser–plasma interaction is simulated in the geometric optics approximation including inverse Bremsstrahlung absorption. At the end of the laser pulse (about 1 ns), the plasma profiles of density, momentum, and temperature from the DUED simulations are remapped onto the 3D Cartesian grid of GORGON. The purpose of this hand-off is to take advantage of the capability of the Lagrangian code to achieve very high resolution in modeling the laser–target interaction. A similar configuration has been used previously.[15–17,33,38]

To remove the axisymmetry imposed by the DUED simulations when remapping onto the GORGON grid, we introduce a uniformly

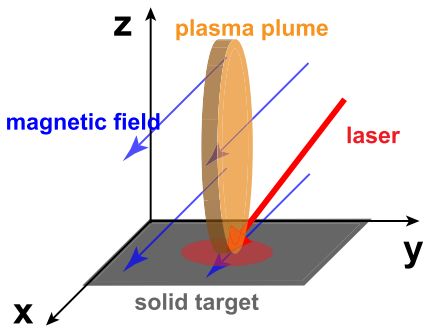

FIG. 1. Schematic of the simulation setup. The solid target is in the xy plane, the direction of the externally applied magnetic field is along the x axis, and the plasma plume expands along the z axis.

distributed random perturbation on the plasma velocity components with maximum amplitude ±5% of the initial value. In addition, to reproduce the kink-like perturbations seen in experiments,[13,33] we impose an asymmetric modulation on the initial plasma velocity between the right and left sides of the slab in Sec. III B. To mimic typical experimental conditions, we also explore Bessel-like modulations, the details of which are given in Sec. III C.

III. 3D SIMULATIONS OF PLASMA EVOLUTION

The global dynamics of the plasma plume over 50 ns are shown in Fig. 2. The initial plasma plume expansion is shown in Fig. 2(a), where we observe the typical diamagnetic cavity and the curved shock envelope that bounds the plasma.[33] The development of the MRTI starts from Fig. 2(b), where the cavity collapses along the y direction and a slab forms from the cavity tip. The development of the flutes and the extension of the slab along the z direction can be seen in Fig. 2(c), where a kink-like instability is already present. The propagation and bending of the slab can be seen in Fig. 2(d).

Figure 3 shows 2D slices of the mass density ρ, electron temperature T_e, and ion temperature T_i of the plasma plume in both the xz and yz planes. On comparing these planes, it is clear that while the plasma plume has been confined in the yz plane, it can freely expand in the xz plane. The detailed plasma parameters are listed in Table I, together with the deduced dimensionless parameters.

We now focus our attention on the collimation of the plasma plume into a slab and on its propagation.

A. Early-time slab formation and MRTI development

In this subsection, we review and extend our previous work[33] to a higher magnetic field of 30 T and an increased perturbation amplitude of the initial momentum on the right-half side of the target. As quantified in Table I, the initial plasma expansion is dominated by the ram pressure, until near-stagnation around 5 ns, and the plasma dynamic beta has a value $\beta_{\mathrm{dyn}} = \rho v^2/[B^2/(2\mu_0)] \sim 22.0$, where v is the fluid velocity, B is the magnetic field strength, and μ_0 is the permeability in vacuum. This would result in an almost-free expansion of the plasma in the xz plane, as detailed in Fig. 4(a). The situation is quite different in the yz plane, as shown in Fig. 4(b). There, the highly conductive plasma plume expands and pushes the magnetic field away. A pressure balance between the ram pressure of the plasma and the ambient magnetic pressure is achieved, and this leads to the end of the diamagnetic cavity expansion.[15] Because the plasma has velocities greater than the fast magneto-acoustic velocity, its deceleration leads to the formation of a curved shock envelope. The magnetosonic Mach number is $M_{\mathrm{ms}} = V_0/\sqrt{c_s^2 + v_A^2} \sim 2.3$, corresponding to a supersonic and super-Alfvénic regime (where c_s is the sound speed and v_A is the Alfvén speed). The plasma in the cavity is redirected along the curved shock toward the z direction, where it forms a conical shock at the tip of the cavity, and a jet-like flow in the yz plane is finally created.[15,16] Note that the tip of the shock envelope is actually not along the $y = 0$ axis: there is a small bending toward the right, as shown by the black velocity arrows. This is due to the initial non-axisymmetric momentum perturbation mentioned above.

The characterization of the shock envelope is detailed in the second column of Table I. The collisionality (the ratio of the mean free path λ_{mfp} to the length scale L_0 of the shock envelope) of both electrons and ions is smaller than unity, confirming the validity of the fluid description.[40] The Hall parameter (representing the magnetization) of electrons is $H_e = \lambda_{\mathrm{mfp},e}/r_{L,e} \sim 5$, indicating that the electrons are magnetized, while the ions are not ($H_i = \lambda_{\mathrm{mfp},i}/r_{L,i} \sim 0.03$).

The MRTI requires an effective acceleration or deceleration at an interface between fluids of different mass density, and this basic condition is met at the interface between the plasma and vacuum when the expanding plasma is halted by the magnetic field lines and also when the cavity collapses.[41] As can be seen in Fig. 5(a), a zoomed view of the structure of the flow along the plasma/vacuum interface reveals the growth of protruding "fingers," which is one of the

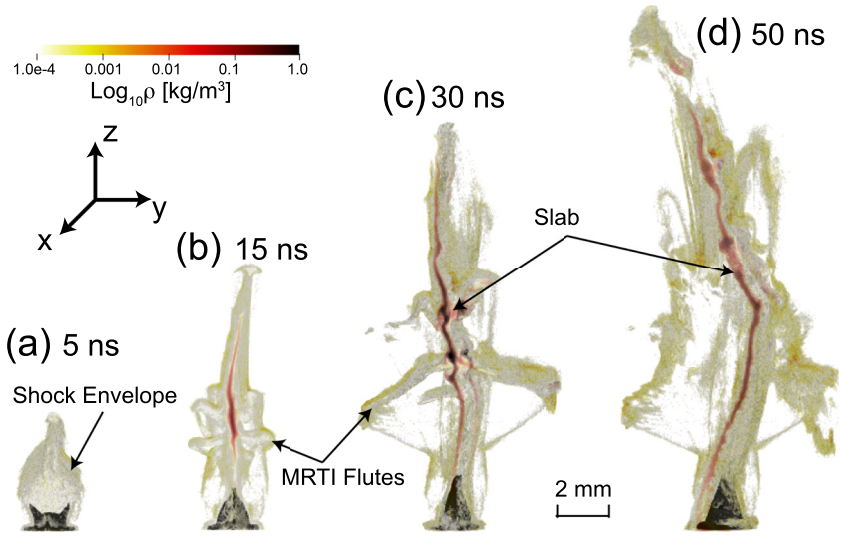

FIG. 2. Plasma dynamics and slab formation. (a)–(d) show global 3D renderings of the decimal logarithm of the mass density at different times (5, 15, 30, and 50 ns) after the laser pulse.

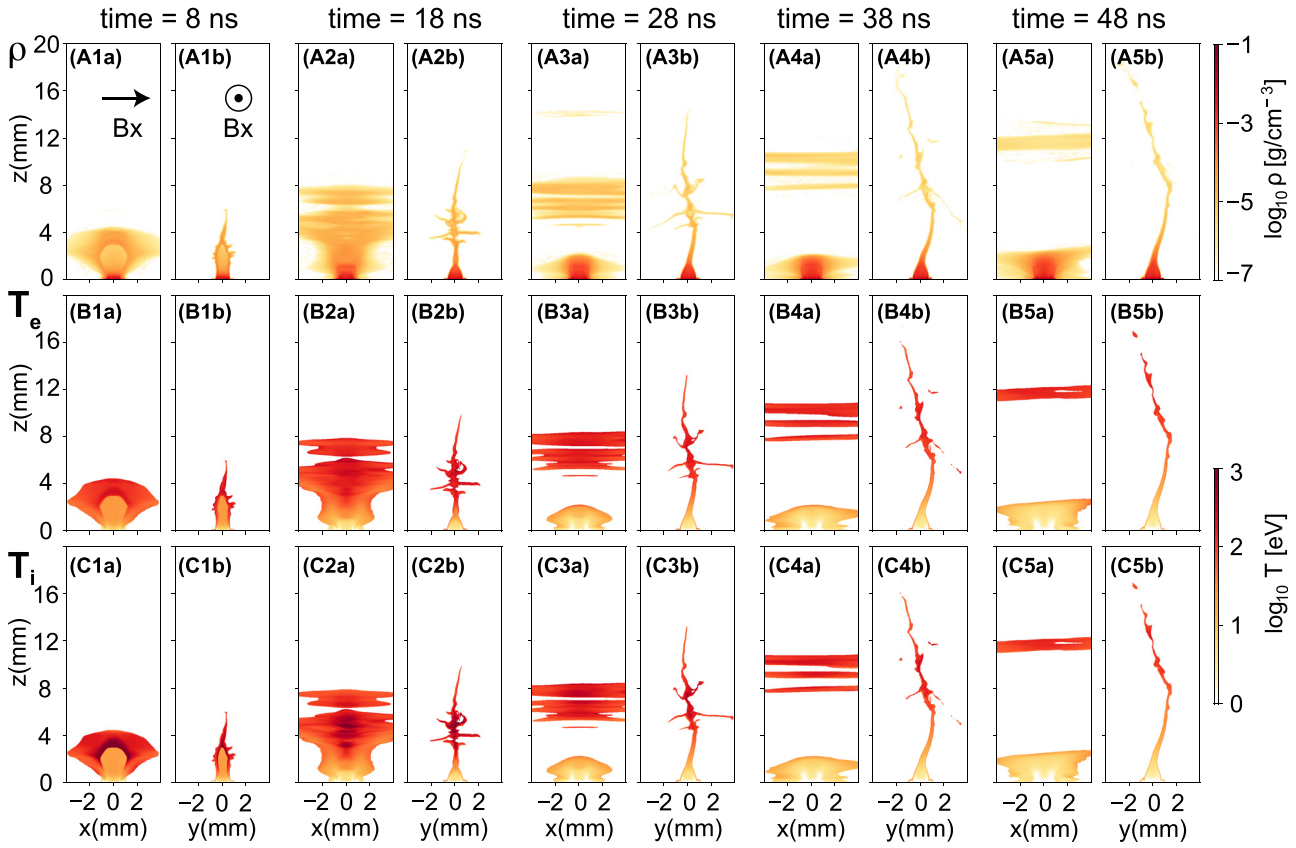

FIG. 3. Decimal logarithm of the mass density ρ (A) and temperatures T_e (B) and T_i (C) of the plasma plume sliced in the middle of the *xz* plane (a) and the *yz* plane (b) at different times 8, 18, 28, 38, and 48 ns (1–5). The temperatures in (B) and (C) share the same color map. The magnetic field directions are shown in (A1a) and (A1b).

characteristics of the MRTI. This will inevitably be triggered if the effective acceleration $g_{\rm eff}$ is antiparallel to the density gradient (in the frame of the interface).

Considering the effect of finite resistivity (which is responsible for damping the MRTI via magnetic field diffusion) and the effect of viscosity (which is responsible for mitigating the growth of the MRTI via sheared velocities at fine scales), we find the maximum of the growth rate to be $\gamma(k) = \sqrt{g_{\rm eff}k - k^2}\,(\eta + \nu)$. Here, η is the magnetic diffusivity; the corresponding term $k^2\eta$ is the electrical resistive contribution to the MRTI dispersion relation; ν is the ion kinematic viscosity; and the corresponding term $k^2\nu$ is the viscosity contribution.[42]

The relative importance of viscosity and resistivity as damping processes can be estimated from the ratio of the above two terms, which also equals the ratio of the magnetic and hydrodynamic Reynolds numbers (i.e., $P = R_m/R_e = \nu/\eta$). Using the Spitzer conductivity[?] and the magnetized ion dynamic viscosity,[40] we obtain $P = 2.2\times10^{-9}\sqrt{\langle A\rangle}T^4/(\Lambda Z_{\rm eff}^5\rho)$, where $\langle A\rangle$ is the averaged atomic number of CF_2, $Z_{\rm eff}$ is the effective charge state, T is the temperature in eV (assuming $T = T_i \sim T_e$), ρ is the mass density in kg/m^3, and Λ is the Coulomb logarithm. With temperatures ranging from 50 to 600 eV (see Fig. 5) in the cavity shell, we find that P ranges from 3×10^{-4} (at 50 eV) to unity (at around 380 eV), and then becomes larger than unity at higher temperature. This indicates that the diffusion term and the viscous term take turns in dominating the MRTI. To take this variation into account, we keep both processes in our estimates, and thus the wavelength of the fastest growing mode considering both resistivity and viscosity can be written as[33]

$$\lambda_{\rm max}\,[\rm mm] \approx \pi g_{\rm eff}^{-1/3}\left(\frac{\sqrt{\langle A\rangle}\,T^{5/2}}{\Lambda Z_{\rm eff}^4\rho} + 7.6\times10^7\frac{\Lambda Z_{\rm eff}}{T^{3/2}}\right)^{2/3}.$$

Furthermore, $g_{\rm eff}$ can be obtained by balancing the Lorentz force and the ram pressure force when the interface stagnates, namely, $\rho g_{\rm eff} \sim jB \sim \nabla P_{\rm ram} \sim \rho v_\perp^2/\delta_{\rm sl}$, where $\delta_{\rm sl}$ is the width of the interface and $v_\perp$ is the local velocity.

In Fig. 5(b), the MRTI growth time and fastest growing mode are calculated using the parameters of our plasma condition at $t = 8$ ns and at the interface, i.e., the mass density $\rho = 0.06$ kg/m^3, the Coulomb logarithm $\Lambda = 9$, the atomic number $\langle A\rangle = 17.32$, the effective charge state $Z_{\rm eff} = 8$, and the effective acceleration $g_{\rm eff} \sim v_\perp^2/\delta_{\rm sl} \sim 3.3\times10^{13}$ m/s^2, in which $\delta_{\rm sl} \sim 300$ μm is the width of the shock envelope and $v_\perp \sim 100$ km/s is the flow velocity. It is clear that over the temperature range of 200–800 eV, as the temperature increases, the wavelength of the fastest growing mode flattens to a narrow band of $\lambda_{\rm max} \sim 1$ mm, and for these modes the characteristic growth time scale is less than ~3 ns, which is consistent with the simulations.

TABLE I. Measured plasma conditions and calculated dimensionless parameters for the case with initial magnetic field $B_{x0} = 30$ T in different regions as indicated in Fig. 2, i.e., the shock envelope at $t = 5$ ns, the MRTI flutes at $t = 30$ ns, and the slab at $t = 50$ ns. $\lambda_{mfp,s}$ (with $s = i$ and e for ions and electrons, respectively) is the mean free path[39] and $r_{L,s}$ is the Larmor radius. The Mach number is the ratio of the flow velocity to the sound velocity, while the Alfvénic Mach number is the ratio of the flow velocity to the Alfvén velocity. The thermal and dynamic beta parameters are the ratios of the plasma thermal and ram pressures, respectively, to the magnetic pressure.

Time	Region	5 ns Shock envelope	30 ns MRTI flutes	50 ns Slab
		Local measurements		
Characteristic length L_0 (μm)		100	100	100
Averaged atomic number A		17.3	17.3	17.3
Effective charge state Z_{eff}		6.5	8.0	8.0
Electron number density n_e (cm^{-3})		1.0×10^{19}	5.0×10^{17}	1.0×10^{18}
Ion number density n_i (cm^{-3})		1.5×10^{18}	7.0×10^{16}	1.5×10^{17}
Mass density ρ (g/cm^3)		4.0×10^{-5}	2.0×10^{-6}	4.0×10^{-6}
Electron temperature T_e (eV)		150.0	120.0	100.0
Ion temperature T_i (eV)		400.0	90.0	100.0
Flow velocity V_0 (km/s)		350.0	150.0	400.0
Magnetic field strength B (T)		25.0	29.0	30.0
		Calculated dimensionless parameters		
Electron collisionality $\lambda_{mfp,e}/L_0$		0.06	0.6	0.2
Ion collisionality $\lambda_{mfp,i}/L_0$		0.1	0.1	0.1
Electron magnetization ($\lambda_{mfp,e}/r_{L,e}$)		5.0	680.0	280.0
Ion magnetization ($\lambda_{mfp,i}/r_{L,i}$)		0.03	0.5	0.3
Mach number M		3.1	1.6	4.7
Alfvénic Mach number M_A		3.3	0.3	1.0
Magnetosonic Mach number M_{ms}		2.3	0.3	1.0
Plasma thermal beta β_{ther}		1.4	3.0×10^{-2}	5.0×10^{-2}
Plasma dynamic beta β_{dyn}		22.0	0.1	2.0

The MRTI initially grows on the outer edges of the cavity, but it also propagates axially along with the flow. After the initial growth phase, Fig. 6(a) shows that at $t = 15$ ns, the density cavity collapses around 3 mm < z < 5 mm, where the MRTI grows rapidly (highlighted by the gray box). At $t = 30$ ns, as shown in Fig. 6(b), the collapsed region propagates along the z direction, arriving at 5 mm < z < 8 mm (also highlighted by a gray box). The MRTI flutes end up merging with each other and elongate along the y direction, reaching $y = 4$ mm. In the meantime, their density is dropping, leaving the plasma plume density compressed around $y = 0$ while propagating along the z direction, thus forming a dense slab structure whose physical parameters are given in the third column of Table I.

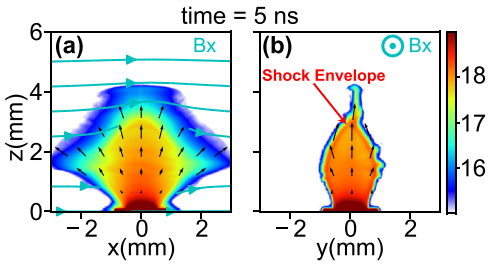

FIG. 4. Plasma expansion and diamagnetic cavity formation: decimal logarithm of the electron number density integrated along or perpendicular to the magnetic field, i.e., the xz plane (a) or the yz plane (b), at 5 ns after the laser ablation. The color map corresponds to $\log_{10}\int n_e\, dy$ in (a) and $\log_{10}\int n_e\, dx$ in (b), in cm^{-2}. The black arrows show the direction and magnitude of the velocities, and the light blue lines and arrows show the direction of the magnetic field in the xz plane (they do not appear as continuous lines, because they are taken out of the sliced plane).

B. Late-time slab bending and magnetic strength effects

We now describe the late-time slab propagation stage, focusing on the kink-like disruption seen, for example, in Figs. 2(c) and 2(d), as well as in Fig. 3, which was clearly observed in recent experiments.[13]

Comparing Figs. 3(A3b) and 3(A4b), it is clear that the propagation of the MRTI flutes (in both the z and y directions) leads to a decrease in their mass density, which eventually drops below the vacuum cutoff employed in the simulations. Thus, at late times, only the central portion of the slab, localized around $y = 0$, is visible. Additionally, we note that in the slab, the electrons and ions have equilibrated to the same temperature. Other parameters, such as the magnetic field and velocity, are listed in Table I.

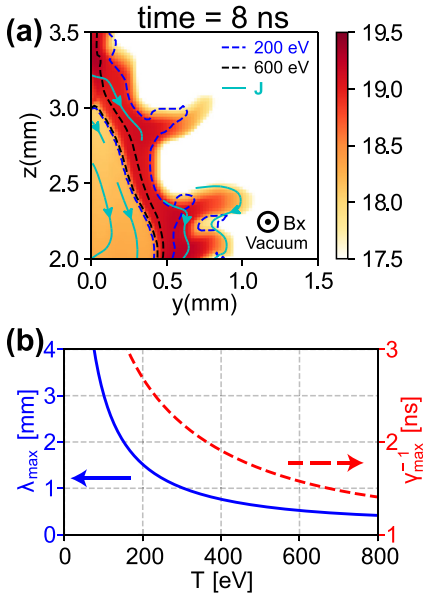

FIG. 5. MRTI growth during slab formation. (a) Zoomed view of the plasma/vacuum interface at $t = 8$ ns. Since the density map here is a slice at the middle plane $x = 0$, the color map corresponds to $\log_{10} n_e$ in cm^{-3}. Cyan lines show the contours of the current density magnitude, while the dashed line contours show the ion temperature T_i. (b) Temperature dependence of the fastest growing mode and the growth time for MRTI.

More interestingly, starting from 28 ns [Figs. 3(A3b)–3(C3b)], it is clear that a kink-like perturbation develops during slab propagation. This bending originates from the asymmetric perturbation introduced initially on the plasma momentum. The purpose of this asymmetric simulation case is to demonstrate that the bending/kinking of the slab can be simply reproduced by perturbing the initial velocity of the plasma plume with a right/left-half imbalance. In the simulation, the choice of the perturbation on the right as being an order of magnitude higher than that on the left is to clearly demonstrate this effect within the simulation time scale.

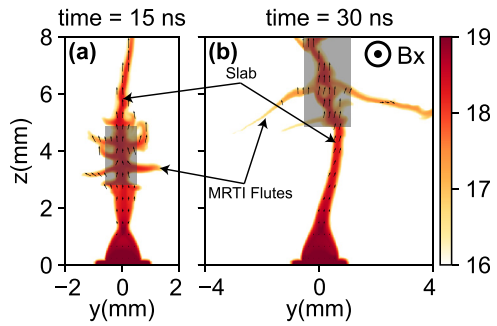

FIG. 6. Slab formation. (a) Collapse of the cavity at $t = 15$ ns around 3 mm $< z <$ 5 mm (highlighted by the gray box). (b) Fully grown flutes at $t = 30$ ns reach the boundary of $y = 4$ mm. The collapsed region propagates along the z direction, arriving at 5 mm $< z <$ 8 mm, and the slab is formed. The color map corresponds to $\log_{10} \int n_e\, dx$ in cm^{-2}. The black arrows are the velocity vectors.

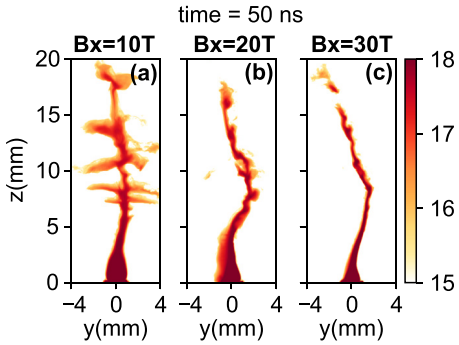

FIG. 7. Slab propagation with different initial magnetic field strengths in the simulation with asymmetric perturbation. (a)–(c) are for $B_{x0} = 10$, 20, and 30 T, respectively. The color map corresponds to $\log_{10} \int n_e\, dx$ in cm^{-2}.

To further investigate the effect of the magnetic field strength on the propagation of the plasma slab, we carried out a series of simulations with a magnetic field increasing from 10 to 30 T and for fixed laser–plasma interaction conditions (i.e., the same as described in Sec. II). The results are compared in Fig. 7. It is clear that as the magnetic field strength is increased, the slab becomes thinner, its density increases, and the amplitude of the kink-like motions becomes more evident. In addition, as the MRTI is more strongly suppressed by a higher magnetic field, the flute structures in the $B_x = 10$ T case are much more obvious than those in the $B_x = 20$ T case. They disappear completely in the $B_x = 30$ T case, because as the magnetic field strength increases, the diamagnetic cavity collapses more quickly, and the MRTI does not have sufficient time to grow.

C. Mimicking the experimental conditions with Bessel-like initial perturbation

Inspired by related laser experiments, where the typical spatial pattern of the laser intensity deposition on target is shown in Fig. 8, we now investigate the effects of the observed ring-like laser-

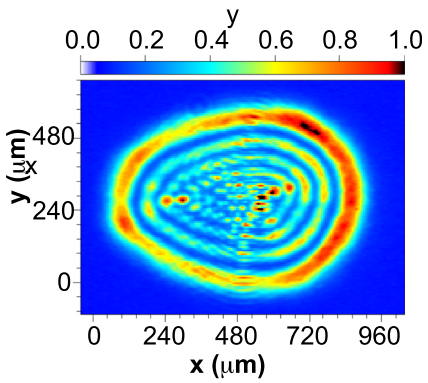

FIG. 8. Typical spatial pattern of the laser intensity deposition on target in related experiments. The pattern is due to the fact that the laser is actually defocused on the plane of the target, so that its intensity is not too large, and hence we have on target a laser pattern with diffraction rings, which is typical of an intermediate plane before focus. The color map represents the normalized intensity.

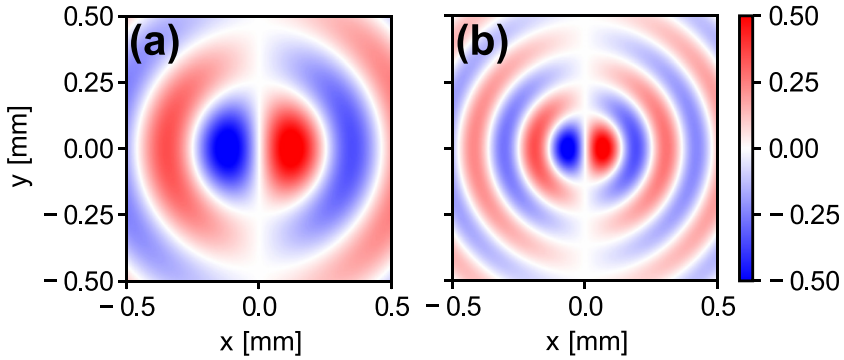

FIG. 9. Spatial distribution of the Bessel-like perturbation of the plasma velocity: (a) $u_{1,1}$, for the $m = 1, n = 1$ mode; (b) $u_{1,2}$, for the $m = 1, n = 2$ mode. Other parameters are $r_0 = 0.5$ mm, $\alpha_{1,1} = 3.8317$, and $\alpha_{1,2} = 7.0156$. The color map corresponds to the perturbation strength.

intensity deposition on the distortions of the slab with a second simulation case. Again, we only perturb the initial velocities in the plasma plume and so mimic the ring-like radial intensity distribution by introducing perturbations of the plasma velocity u with the Bessel-like form

$$u_{mn}(r,\theta) = J_m\left(\frac{\alpha_{mn}}{r_0}r\right)\sin(m\theta),$$

where $r = \sqrt{x^2 + y^2}$ is the distance to the circle of the laser spot on the target surface (x and y are the spatial coordinates), the angle $\theta = \arctan(y/x)$, J_m is the Bessel function of the first kind, α_{mn} is the nth root of J_m, and r_0 is the laser spot radius, as illustrated in Fig. 9.

We note that in these simulations, there is no added right/left asymmetry, as was the case for the simulations presented in Sec. III B. Here, we compare the results for two of the above perturbation modes, namely, $m = 1$, $n = 1$ and $m = 1$, $n = 2$, for different magnetic field strengths, namely, $B_x = 10$ and 30 T, at $t = 50$ ns. For $B_x = 10$ T, a comparison of Figs. 10(a) and 10(b) reveals no obvious difference between slab propagation with initial Bessel-like perturbation in the $m = 1$, $n = 1$ mode and propagation with initial perturbation in the $m = 1, n = 2$ mode. In both cases, there is weak slab bending along the z direction, and a fairly large number of flute structures are still present. However, for $B_x = 30$ T, in Figs. 10(c) and 10(d), distinct differences can be seen between the modes. Besides the bending of the slab, we also see the formation of kink-like disruption, with patterns that are much stronger for an initial perturbation in the $m = 1, n = 2$ mode than in the $m = 1$, $n = 1$ mode. This disruption leads to a shorter propagation distance in the case of the $m = 1$, $n = 2$ mode than the $m = 1$, $n = 1$ mode. The kink-like disruptions in both cases for $B_x = 30$ T are clearly stronger than those for $B_x = 10$ T. Note that the simulations shown here are different from the case shown in Figs. 3(A5b)–3(C5b), where the perturbations had no ring-like structure. This further indicates that the particular pattern of the laser spot inhomogeneity plays a crucial role in determining the pattern and level of the kink-like disruptions. As mentioned above, this is also in accordance with recent experimental observations.[13]

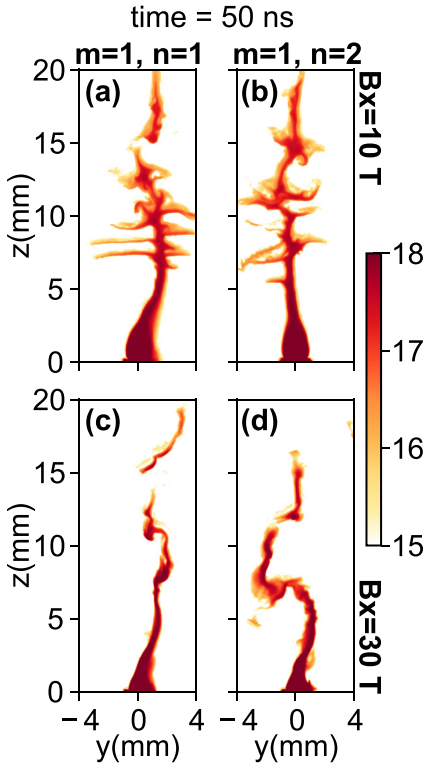

FIG. 10. Slab propagation with different modes of Bessel-like perturbation for different magnetic field strengths at the end of the simulation at $t = 50$ ns. The color map corresponds to $\log_{10}\int n_e\,dx$ in cm^{-2}, i.e., to the decimal logarithm of the electron number density integrated along the external magnetic field. (a) and (b) are for $B_x = 10$ T, while (c) and (d) are for $B_x = 30$ T. In (a) and (c), the initial Bessel-like perturbation is in the $m = 1$, $n = 1$ mode, while in (b) and (d), it is in the $m = 1$, $n = 2$ mode.

IV. CONCLUSIONS

A detailed characterization of the overall stability and dynamics of a laser-produced plasma across a magnetic field of tens of teslas has been investigated with large-scale 3D resistive-MHD simulations. It has been found that the plasma is first collimated by the magnetic field into a slender slab, whose plasma–vacuum interface is dominated by the MRTI. Later, the flutes fade away, and the plasma elongates, forming a slab-like structure. We have shown that during its

propagation, the slab undergoes kink-like disruptions because of the imbalance of the initial perturbation, which originates from the inhomogeneity of the laser-intensity deposition. By mimicking the pattern of a typical laser-intensity profile from related experiments using a Bessel-like function, we find that the kink-like structures observed in the slab arise from the initial velocity perturbations that are imposed, and their amplitude increases with increasing strength of the magnetic field.

ACKNOWLEDGMENTS

This work was supported by funding from the European Research Council (ERC) under the European Union's Horizon 2020 research and innovation program (Grant Agreement No. 787539). The research leading to these results is supported by Extreme Light Infrastructure Nuclear Physics (ELI-NP) Phase II, a project co-financed by the Romanian Government and European Union through the European Regional Development Fund, and by the Project No. ELI-RO-2020-23 funded by IFA (Romania). This work was also granted access to the HPC resources of MesoPSL financed by the Region Ile de France and the project Equip at Meso (Reference No. ANR-10-EQPX-29-01) of the program Investissements d'Avenir supervised by the National Agency for Research.

AUTHOR DECLARATIONS

Conflict of Interest

The authors declare no competing interests.

DATA AVAILABILITY

All data needed to evaluate the conclusions in the paper are present in the paper. Simulation data is archived on the servers at LERMA laboratories, and is available from the corresponding author upon reasonable request.

REFERENCES

[1]P. A. Bernhardt, R. A. Roussel-Dupre, M. B. Pongratz, G. Haerendel, A. Valenzuela, D. A. Gurnett, and R. R. Anderson, "Observations and theory of the AMPTE magnetotail barium releases," J. Geophys. Res.: Space Phys. **92**, 5777–5794 (1987).

[2]S. Fujioka, Z. Zhang, K. Ishihara, K. Shigemori, Y. Hironaka, T. Johzaki, A. Sunahara, N. Yamamoto, H. Nakashima, T. Watanabe *et al.*, "Kilotesla magnetic field due to a capacitor-coil target driven by high power laser," Sci. Rep. **3**, 1170 (2013).

[3]B. Albertazzi, J. Béard, A. Ciardi, T. Vinci, J. Albrecht, J. Billette, T. Burris-Mog, S. N. Chen, D. Da Silva, S. Dittrich *et al.*, "Production of large volume, strongly magnetized laser-produced plasmas by use of pulsed external magnetic fields," Rev. Sci. Instrum. **84**, 043505 (2013).

[4]G. Revet, S. N. Chen, R. Bonito, B. Khiar, E. Filippov, C. Argiroffi, D. P. Higginson, S. Orlando, J. Béard, M. Blecher *et al.*, "Laboratory unraveling of matter accretion in young stars," Sci. Adv. **3**, e1700982 (2017).

[5]D. B. Schaeffer, W. Fox, D. Haberberger, G. Fiksel, A. Bhattacharjee, D. H. Barnak, S. X. Hu, K. Germaschewski, and R. K. Follett, "High-Mach number, laser-driven magnetized collisionless shocks," Phys. Plasmas **24**, 122702 (2017).

[6]Y. Kuramitsu, T. Moritaka, Y. Sakawa, T. Morita, T. Sano, M. Koenig, C. D. Gregory, N. Woolsey, K. Tomita, H. Takabe *et al.*, "Magnetic reconnection driven by electron dynamics," Nat. Commun. **9**, 5109 (2018).

[7]W. Yao, A. Fazzini, S. N. Chen, K. Burdonov, P. Antici, J. Béard, S. Bolaños *et al.*, "Laboratory evidence for proton energization by collisionless shock surfing," Nat. Phys. **17**(10), 1177–1182 (2021).

[8]W. Yao, A. Fazzini, S. N. Chen, K. Burdonov, P. Antici, J. Béard, S. Bolaños *et al.*, "Detailed characterization of a laboratory magnetized supercritical collisionless shock and of the associated proton energization," Matter Radiat. Extremes **7**(1), 014402 (2022).

[9]K. Burdonov, W. Yao, A. Sladkov, R. Bonito, S. N. Chen, A. Ciardi, A. Korzhimanov *et al.*, "Laboratory modelling of equatorial 'tongue'accretion channels in young stellar objects caused by the Rayleigh-Taylor instability," Astron. Astrophys. **657**, A112 (2022).

[10]A. Fazzini, W. Yao, K. Burdonov, J. Béard, S. N. Chen, A. Ciardi, E. d'Humières *et al.*, "Particle energization in colliding subcritical collisionless shocks investigated in the laboratory," arXiv:2202.03465 (2022).

[11]S. A. Slutz and R. A. Vesey, "High-gain magnetized inertial fusion," Phys. Rev. Lett. **108**, 025003 (2012).

[12]J. R. Davies, D. H. Barnak, R. Betti, E. M. Campbell, P.-Y. Chang, A. B. Sefkow, K. J. Peterson, D. B. Sinars, and M. R. Weis, "Laser-driven magnetized liner inertial fusion," Phys. Plasmas **24**, 062701 (2017).

[13]E. D. Filippov, S. S. Makarov, K. F. Burdonov, W. Yao, G. Revet, J. Béard, S. Bolaños, S. N. Chen, A. Guediche, J. Hare *et al.*, "Enhanced x-ray emission arising from laser-plasma confinement by a strong transverse magnetic field," Sci. Rep. **11**, 8180 (2021).

[14]D. Froula, J. Ross, B. Pollock, P. Davis, A. James, L. Divol, M. Edwards, A. Offenberger, D. Price, R. Town *et al.*, "Quenching of the nonlocal electron heat transport by large external magnetic fields in a laser-produced plasma measured with imaging Thomson scattering," Phys. Rev. Lett. **98**, 135001 (2007).

[15]A. Ciardi, T. Vinci, J. Fuchs, B. Albertazzi, C. Riconda, H. Pépin, and O. Portugall, "Astrophysics of magnetically collimated jets generated from laser-produced plasmas," Phys. Rev. Lett. **110**, 025002 (2013).

[16]B. Albertazzi, A. Ciardi, M. Nakatsutsumi, T. Vinci, J. Béard, R. Bonito, J. Billette, M. Borghesi, Z. Burkley, S. N. Chen *et al.*, "Laboratory formation of a scaled protostellar jet by coaligned poloidal magnetic field," Science **346**, 325–328 (2014).

[17]D. P. Higginson, G. Revet, B. Khiar, J. Béard, M. Blecher, M. Borghesi, K. Burdonov, S. N. Chen, E. Filippov, D. Khaghani *et al.*, "Detailed characterization of laser-produced astrophysically-relevant jets formed via a poloidal magnetic nozzle," High Energy Density Phys. **23**, 48–59 (2017).

[18]C. Plechaty, R. Presura, and A. A. Esaulov, "Focusing of an explosive plasma expansion in a transverse magnetic field," Phys. Rev. Lett. **111**, 185002 (2013).

[19]A. N. Mostovych, B. H. Ripin, and J. A. Stamper, "Laser produced plasma jets: Collimation and instability in strong transverse magnetic fields," Phys. Rev. Lett. **62**, 2837 (1989).

[20]J. Bruneteau, E. Fabre, H. Lamain, and P. Vasseur, "Experimental investigation of the production and containment of a laser-produced plasma," Phys. Fluids **13**, 1795–1801 (1970).

[21]T. Matoba and S. Ariga, "Motion and collision of plasma blobs produced by giant pulse laser in a transverse magnetic field," J. Phys. Soc. Jpn. **30**, 1477–1487 (1971).

[22]G. Jellison and C. Parsons, "Resonant shadowgraph and schlieren studies of magnetized laser-produced plasmas," Phys. Fluids **24**, 1787–1790 (1981).

[23]S. Okada, K. Sato, and T. Sekiguchi, "Behaviour of laser-produced plasma in a uniform magnetic field–plasma instabilities," Jpn. J. Appl. Phys. **20**, 157 (1981).

[24]B. H. Ripin, E. A. McLean, C. K. Manka, C. Pawley, J. A. Stamper, T. A. Peyser, A. N. Mostovych, J. Grun, A. B. Hassam, and J. Huba, "Large-Larmor-radius interchange instability," Phys. Rev. Lett. **59**, 2299 (1987).

[25]B. H. Ripin, J. D. Huba, E. A. McLean, C. K. Manka, T. Peyser, H. R. Burris, and J. Grun, "Sub-Alfvénic plasma expansion," Phys. Fluids B **5**, 3491–3506 (1993).

[26]D. Winske, "Development of flute modes on expanding plasma clouds," Phys. Fluids B **1**, 1900–1910 (1989).
[27]J. D. Huba, A. B. Hassam, and D. Winske, "Stability of sub-Alfvénic plasma expansions," Phys. Fluids B **2**, 1676–1697 (1990).
[28]T. A. Peyser, C. K. Manka, B. H. Ripin, and G. Ganguli, "Electron–ion hybrid instability in laser-produced plasma expansions across magnetic fields," Phys. Fluids B **4**, 2448–2458 (1992).
[29]A. B. Hassam and J. D. Huba, "Nonlinear evolution of the unmagnetized ion Rayleigh–Taylor instability," Phys. Fluids B **2**, 2001–2006 (1990).
[30]Y. P. Zakharov, V. M. Antonov, E. L. Boyarintsev, A. V. Melekhov, V. G. Posukh, I. F. Shaikhislamov, and V. V. Pickalov, "Role of the Hall flute instability in the interaction of laser and space plasmas with a magnetic field," Plasma Phys. Rep. **32**, 183–204 (2006).
[31]H.-b. Tang, G.-y. Hu, Y.-h. Liang, Y.-l. Wang, T. Tao, P. Hu, P. Yuan, P. Zhu, Y. Zuo, B. Zhao *et al.*, "Observation of large Larmor radius instability in laser plasma expanding into a 10 T external magnetic field," Phys. Plasmas **27**, 022108 (2020).
[32]C. Plechaty, R. Presura, S. Stein, D. Martinez, S. Neff, V. Ivanov, and Y. Stepanenko, "Penetration of a laser-produced plasma across an applied magnetic field," High Energy Density Phys. **6**, 258–261 (2010).
[33]B. Khiar, G. Revet, A. Ciardi, K. Burdonov, E. Filippov, J. Béard, M. Cerchez, S. N. Chen, T. Gangolf, S. S. Makarov *et al.*, "Laser-produced magnetic-Rayleigh-Taylor unstable plasma slabs in a 20 T magnetic field," Phys. Rev. Lett. **123**, 205001 (2019).
[34]J. P. Chittenden, S. V. Lebedev, C. A. Jennings, S. N. Bland, and A. Ciardi, "X-ray generation mechanisms in three-dimensional simulations of wire array Z-pinches," Plasma Phys. Controlled Fusion **46**, B457 (2004).
[35]A. Ciardi, S. V. Lebedev, A. Frank, E. G. Blackman, J. P. Chittenden, C. J. Jennings, D. J. Ampleford, S. N. Bland, S. C. Bott, J. Rapley *et al.*, "The evolution of magnetic tower jets in the laboratory," Phys. Plasmas **14**, 056501 (2007).
[36]G. Revet, "Modelling magnetized accretion columns of young stars in the laboratory," Ph.D. thesis, Université Paris-Saclay (ComUE), 2018.
[37]S. Atzeni, A. Schiavi, F. Califano, F. Cattani, F. Cornolti, D. Del Sarto, T. V. Liseykina, A. Macchi, and F. Pegoraro, "Fluid and kinetic simulation of inertial confinement fusion plasmas," Comput. Phys. Commun. **169**, 153–159 (2005).
[38]D. P. Higginson, B. Khiar, G. Revet, J. Béard, M. Blecher, M. Borghesi, K. Burdonov, S. N. Chen, E. Filippov, D. Khaghani *et al.*, "Enhancement of quasistationary shocks and heating via temporal staging in a magnetized laser-plasma jet," Phys. Rev. Lett. **119**, 255002 (2017).
[39]B. Trubnikov, "Particle interactions in a fully ionized plasma," Rev. Plasma Phys **1**, 105–140 (1965).
[40]D. Ryutov, R. P. Drake, J. Kane, E. Liang, B. A. Remington, and W. M. Wood-Vasey, "Similarity criteria for the laboratory simulation of supernova hydrodynamics," Astrophys. J. **518**, 821 (1999).
[41]B. Khiar, "Laboratory astrophysics with magnetized laser-produced plasmas," Ph.D. theses, Université Pierre et Marie Curie–Paris VI, 2017.
[42]T. S. Green and G. B. F. Niblett, "Rayleigh-Taylor instabilities of a magnetically accelerated plasma," Nucl. Fusion **1**, 42 (1960).